Available online at www.sciencedirect.com
ScienceDirect
C. R. Mecanique 337 (2009) 504–516
COMPTES RENDUS MECANIQUE

Combustion for aerospace propulsion

# Laser-based measurements of gas-phase chemistry in non-equilibrium pulsed nanosecond discharges

Frédéric Grisch *, Guy-Alexandre Grandin, Dominique Messina, Brigitte Attal-Trétout

*Office national d'études et de recherches aérospatiales, Fort de Palaiseau, 91761 Palaiseau cedex, France*

Available online 24 July 2009

**Abstract**

Detailed experimental investigation of a non-equilibrium nanosecond pulsed discharge in premixed $CH_4$/air mixtures at atmospheric pressure has been carried out. The experiments demonstrated significant reductions in ignition delay and increased lean burn capability relative to conventional spark ignition. Advanced laser diagnostics have been used to identify the physical processes which lead to these improvements. The electron temperature and density properties were measured using laser Thomson scattering (LTS). Temperature measurements were performed using $N_2$ CARS thermometry to quantify the energy transfer in the gas mixture. Effect of the discharge on the local temperature shows the existence of the ignition of the gas mixture for equivalence ratio between 0.7 and 1.3. Fast development of a flame kernel is then observed. The experiment also shows that the flame can be sustained above the discharge due the repetitive ignition of the flame at the plasma repetition rate. Finally, OH and CH PLIF experiments were performed to confirm the large OH and CH streamer-induced production over the discharge volume. ***To cite this article: F. Grisch et al., C. R. Mecanique 337 (2009).***



**Résumé**

**Analyse expérimentale des mécanismes physico-chimiques de décharges nanosecondes impulsionnelles répétitives par diagnostics lasers avancés.** L'analyse expérimentale de l'effet d'une décharge nanoseconde impulsionnelle répétitive dans un mélange gazeux $CH_4$/air à pression atmosphérique a été entreprise. Les expériences révèlent une réduction significative des délais d'allumage ainsi qu'une amélioration de la combustion en mélange pauvre comparées à celles obtenues suite à un allumage par bougie conventionnelle. L'analyse de ces processus physiques a été analysée au moyen de diagnostics lasers avancés. La température des électrons et la densité électronique ont été mesurées par diffusion laser Thomson (LTS). Des mesures de température, nécessaires pour quantifier les transferts d'énergie entre la décharge et la mélange gazeux, ont été réalisées par thermométrie DRASC sur la molécule d'azote. L'augmentation de la température des molécules neutres par la décharge entraîne un allumage du mélange gazeux dans la gamme de richesse 0.7–1.3, puis s'ensuit un rapide développement d'une flamme de type Kernel. Les expériences révèlent également que la flamme est auto entretenue au dessus de la décharge grâce à l'allumage répétitif induit par la cadence de répétition de production de la décharge. Finalement, les radicaux OH et CH ont été dosés par fluorescence induite par laser (PLIF). La large production de ces espèces dans les premiers instants de l'application de la décharge confirme le potentiel de cette décharge dans le changement des mécanismes chimiques nécessaire en vue de l'amélioration des processus de combustion. ***Pour citer cet article : F. Grisch et al., C. R. Mecanique 337 (2009).***



* Corresponding author.
*E-mail address:* frederic.grisch@onera.fr (F. Grisch).

1631-0721/$ – see front matter 
doi:10.1016/j.crme.2009.06.021

*Keywords:* Combustion; Nanosecond discharge; Ignition; Laser diagnostic; Electron; Temperature; OH; CH

*Mots-clés :* Combustion ; Décharge impulsionnelle nanoseconde ; Allumage ; Diagnostic laser ; Température ; Électron ; OH ; CH

## 1. Introduction

Control of ignition and combustion processes in aircraft jet engines is of crucial importance for their performance and reliability. Reduction of ignition delay, flame-holding and flame stability improvement, flame blow-off prevention and extension of flammability limits are some of the key technical issues which are generally controlled, with limited success, by methods based on conventional thermal ignition systems (arc discharge, ...). An alternative method consists on modifying the chemical reaction kinetics by generating and sustaining large electron number densities, which results in a non-equilibrium excitation of the gas mixture. Better efficiency of population transfer within electronic and vibrational states can be obtained using pulsed nanosecond discharges which handle a reduced electric field [1–5].

Over the last few years, considerable progress has been made in understanding non-equilibrium plasma-assisted combustion. Recent experimental work focused of nanosecond pulse duration discharges on various phenomena such as reduction of ignition delay [6], flame stabilization [7–9], ignition and flame holding [10–12]. However, the processes of energy transfer between the plasma and the gas medium remain not fully understood. They, however, represent a key issue to improve the understanding of the main physical processes governing the discharge–flame interaction. In this context, experimental data characterizing the thermodynamic and kinetic processes occurring in these discharges need to be obtained. More specifically, population distributions of neutral molecules and species composition are important quantities which can be used as input parameters for the simulation of this interaction. Elucidating the thermodynamic and kinetic mechanisms of fuel oxidation and ignition by a nanosecond pulsed discharge is then the main objective of the present work.

In the present experiments, a high voltage, nanosecond pulse duration, capacitively coupled discharge sustained in atmospheric premixed methane–air flows has been studied. The probing of the pulsed discharge has been performed by using laser diagnostics which enable locally and temporally resolved measurements of temperature and species concentration. Among these techniques, coherent anti-Stokes Raman scattering (CARS), Planar Laser-Induced Fluorescence (PLIF) and laser Thomson scattering (LTS) have been specifically developed and applied to characterize this type of discharge. CARS is used to measure, within the plasma produced in pure air and in various methane/air mixtures, the population distribution of $N_2$ in its ground electronic state. Temporal evolution of these populations is recorded by delaying the laser shots relative to the discharge pulse (from 10 ns to 1 ms). Experiments were also carried out in premixed $CH_4$/air flames to study the effect of a nanosecond pulse discharge on flame ignition and stabilization at atmospheric pressure. These results were used to assess the feasibility of temperature single-shot measurements with CARS in order to get an insight into the thermodynamics and kinetic properties of discharges in hydrocarbon/air mixtures. This work was completed by probing the temporal methane oxidation as well as the kinetic mechanism of recombination of radicals and atoms into neutral molecules such as $H_2$ and $C_2H_2$. PLIF has been also applied to detect primary radical species concentration (OH and CH) produced by the pulsed discharge. Finally, laser Thomson scattering has been implemented to measure the electron properties of the discharge such as electron density and electron temperature.

## 2. Experimental set-up

A non-equilibrium plasma is produced by a repetitive pulse generator allowing to generate negative electric pulses ranging from $-10$ to $-40$ kV in amplitude, 70 ns in duration with a pulse repetition frequency up to 200 Hz [13]. The high-voltage pulse generator is built using a hydrogen dual-grid thyratron for better triggering speed, with a hollow cathode for protection against voltage reflections. Triggering synchronization, obtained with a pulse/delay generator, allows one to achieve a temporal jitter as low as 10 ns which is very appropriate to the synchronization of laser diagnostic measurements with the pulsed discharge. Two stainless-steel needles, with a curvature radius at the tip of 0.1 mm are placed above the nozzle exit to produce the pulsed discharge. Positions of the needles with respect to the nozzle could be varied horizontally and vertically. Both electrodes are tilted vertically by 8.8 degrees with respect to the propagation of the laser beams in the discharge. This arrangement allows the laser beams to be focused at

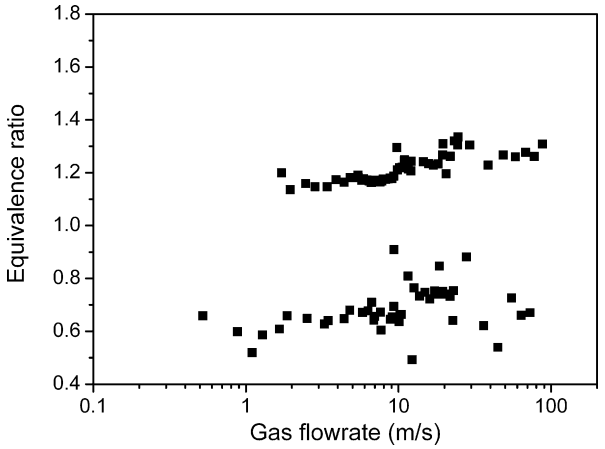


Fig. 1. Evolution of the upper and lower limits of ignition.

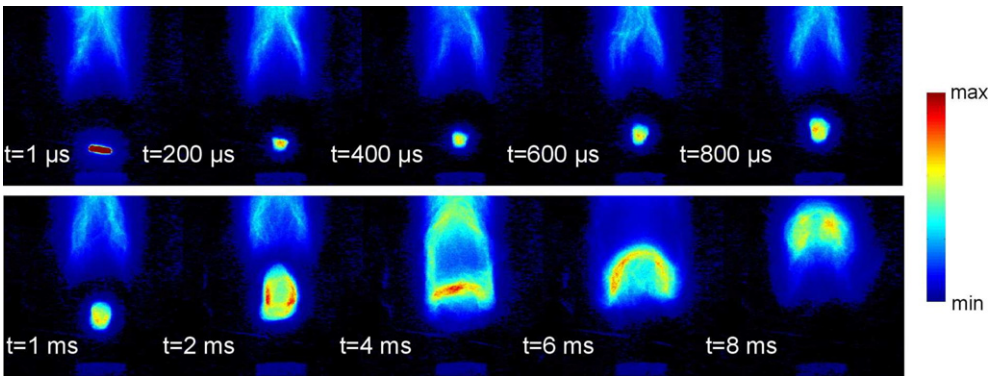


Fig. 2. Time evolution of the mean structure of the flame using the $OH^*$ chemiluminescence. Each image is the average of 20 instantaneous images recorded with a temporal gate of 10 µs.

the centre of the discharge. The burner consists of two concentric nozzles made of ceramics which is an electrically non-conductive material used to avoid electrical disturbances of the discharge. The inner injection nozzle is 10 mm diameter and is surrounded by an annular nozzle which is 20 mm in diameter. Depending on the experiments, the inner nozzle operates with a methane/air mixture with variable composition, while inert gas is injected through the surrounding nozzle to prevent chemical and hydrodynamical disturbances of the inner flow. Mass flowmeters are used to adjust accurately the different flowrates.

### *2.1. Operating regimes of ignition and flame stabilization*

The operating regimes of a methane–air flow at atmospheric pressure have been determined, as a function of equivalence ratio ($\Phi$) and airflow rate. Measurements performed at different bulk flow velocities reveal the efficiency of the plasma for improving the ignition of a $CH_4$–air mixture. For instance, Fig. 1 depicts the upper and lower limits of the equivalence ratio between which ignition and flame development were systematically observed for inlet bulk velocities ranging from 1 to 70 m/s. In these experiments, the energy deposited by the plasma in the gas mixture is fixed to 0.8 mJ/pulse and with a repetition rate of 100 Hz. It is noted that ignition typically occurs in the 0.7–1.3 equivalence ratio range. At higher inlet bulk velocity, i.e. between 70 and 100 m/s, ignition still occurs but extinction of the flame rapidly appears, reducing then the effect of the plasma on the gas mixture.

In the case where the bulk flow velocity is lower than 70 m/s, the development of a flame downstream from the electrodes is observed after ignition. Fig. 2 presents an example of the temporal evolution of the flame structure over a discharge cycle ($\Delta t = 10$ ms) recorded at $\Phi = 0.95$ for a bulk velocity of the fresh gases of 3 m/s. Each picture in

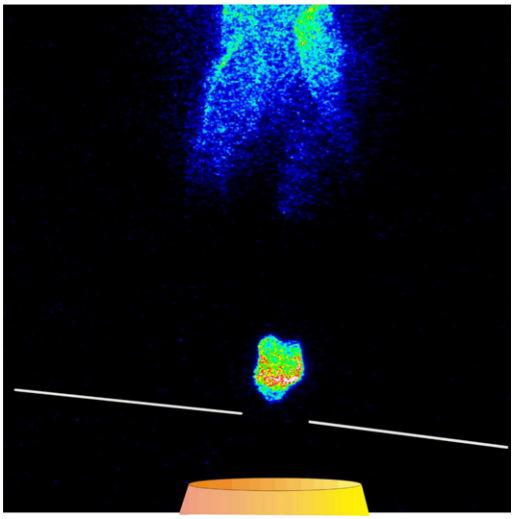

Fig. 3. Instantaneous image of the structure of the flame kernel recorded at $\Delta t = 600$ µs.

Fig. 2 corresponds to the average over 20 instantaneous images of OH* chemiluminescence recorded with a temporal gate of 10 µs which and at various delays after the discharge. The images are recorded on the two first centimeters spatial zone located downstream from the electrodes. In these conditions, ignition of the gas mixture is found to be very fast, typically about 500 ns which corroborate the potentialities of the pulsed discharge for fast and efficient chemical modification on the fresh gas mixture. The first row in Fig. 2 shows the early development of the flame kernel initiated by the plasma discharge which is initially 3 mm long and 200 µm in diameter. The flame kernel grows up rapidly with a velocity of about 3 m/s in a quasi-spherical manner. It should be noticed that, as these pictures are averaged, the shape of the flame kernel appears to be smooth. However, instantaneous OH* images show that the flame front is highly wrinkled by turbulence (Fig. 3). It is also noted that OH* chemiluminescence intensity is much larger in the flame kernel than in the typical conical shape of the flame zone (upper part of each picture) resulting from the combustion coming from the preceding cycle. This phenomenon seems to be due to higher strain rate in the flame kernel and additional chemical reactions resulting in enhanced flame reaction rate. Furthermore, integration of the chemiluminescence intensity over the line-of-sight can also bias the signal recorded by the ICCD camera. Especially important are the small dimensions of the kernel which clearly lie within the lens depth-of-field.

The four pictures on the right in the second row of Fig. 2 correspond to the development of the flame kernel at later stages of the discharge cycle. Interesting information can be obtained from these pictures. At $t = 2$ ms, the flame kernel has considerably grown up and is located very close to the $CH_4$/air flame resulting from the preceding cycle. Flame front at the surface of the kernel is materialized by the two zones with intense intensity at each edge of the kernel, while intensity within the kernel (corresponding to hot gases) is lower. At $t = 4$ ms, the flame kernel exhibits a double structure, where both parts tend to separate from each other. One part seems to remain fairly horizontal at the bottom of the kernel while the second part is transported by the fresh gaseous mixture to the $CH_4$/air flame. Regions with lower OH* chemiluminescence intensity can be noticed between upper and lower parts of the kernel, which is possibly due to entrainment of surrounding air into the jet, resulting into dilution of the $CH_4$/air mixture, hence reduced reaction rate. At $t = 6$ ms, the lower part of the initial flame kernel exhibits a hemispherical shape coming from the recirculation of surrounding air into the jet, which tends to distort the flame front along the jet bulk direction. Finally at $t = 8$ ms, a mushroom-like structure of the initial flame kernel with two zones of intense OH* chemiluminescence intensity is observed. It is interesting to notice that the two tails located below the mushroom head have the same spatial extent that the conical structure of the $CH_4$/air flame. This suggests that this structure is the result (or the residue) of the transport of the mushroom flame within the flowfield.

Measurements performed at various plasma repetition rates also reveal the influence of the energy deposited per unit time by the discharge on flame efficiency. For instance, Fig. 4 displays average flame emission images recorded for $\Phi = 0.95$ at plasma repetition rates ranging from 33 to 200 Hz. Assuming that the flame length corresponds to a 100% combustion rate, the increase of the plasma repetition rate controlling the energy deposited by the plasma per

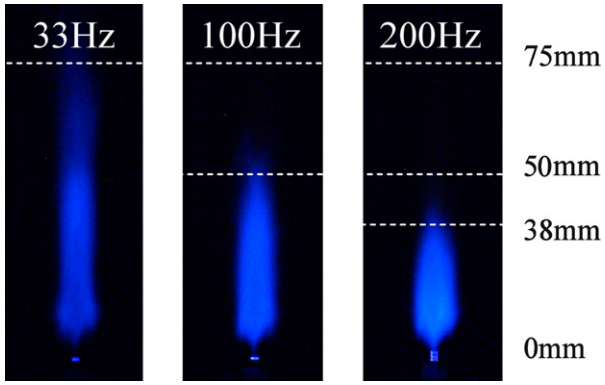


Fig. 4. Flame length for various plasma repetition rates.

unit time significantly improves the combustion efficiency. The length of the flame then decreases with the increase of the repetition rates probably due to larger heat release. All these results significantly demonstrate the positive effects of nanosecond pulsed discharges on the enhancement of ignition and combustion of $CH_4$/air mixtures. In order to get a better comprehension of the interaction between the plasma and the gas mixture, advanced laser diagnostics were employed to characterize the plasma properties and study the thermal and chemical mechanisms leading to these physical processus.

## 3. Electron properties

### *3.1. Laser Thomson scattering*

Laser Thomson scattering (LTS) has been widely used as a powerful plasma diagnostic tool which offers the potential of determining detailed information about electron number density ($n_e$) and electron temperature ($T_e$) [14]. LTS is a non-perturbing optical method based on the scattering of laser radiation by free charged particles, when the energy of an incident photon is much less than the particles rest energy. The energy lost by the radiation is accounted for by the classical theory as a result of the radiation emitted by the charged particles when they are accelerated in the transverse electric field of the radiation. Because ions are much heavier than electrons, their scattering intensity is usually small enough to be negligible and only scattering by electrons is considered in the following. The principle and general experimental arrangement of LTS have been described in detail in many textbooks [15–17]. Without going in detail, the total electric field induced by Thomson scattering by the plasma is defined as the vector sum of the field of each individual electron in the scattering volume [15]. To do this correctly, both the scattering cross section of the single electrons and the phase relation between the scattered waves has to be taken into account. Correlated interactions between the plasma electrons only occur above a certain scale length, the so-called Debye length, $\lambda_D = 7.4 \times 10^3 \sqrt{T_e/n_e}$. Whether collective electron phenomena influence the scattering process depends on the ratio between $\lambda_D$ and the wavelength ($\lambda_0$) of the incident electromagnetic wave, which is expressed as the Salpeter (or scattering) parameter $\alpha$

$$\alpha = (k\lambda_D)^{-1} = \frac{\lambda_0}{4\pi\lambda_D \sin(\theta/2)} \tag{1}$$

where $k$ refers to the differential scattering vector and $\theta$ is the angle between the incident wave and scattered wave functions. When $\alpha \ll 1$, the wavelength of the incident laser photon is short compared to the average distance between electrons. The photon "sees" the electron as an individual particle, randomly distributed. The phases of all contributions are completely uncorrelated and the resultant scattering intensity is just the summation of intensity contributions of each individual electron. This physical process is then refereed as the incoherent Thomson scattering. On the other hand, if the average distance is short compared to the laser wavelength, the phase difference is no longer random and the individual electron scattering will add up coherently. This gives a lineshape which is different from incoherent scattering. This phenomenon is then called coherent Thomson scattering. In the present case, typical values of electron density ($n_e = 1 \times 10^{18}$ m$^{-3}$) and electron temperature ($T_e = 3$ eV) lead to $\alpha = 0.02$ when the laser wavelength is

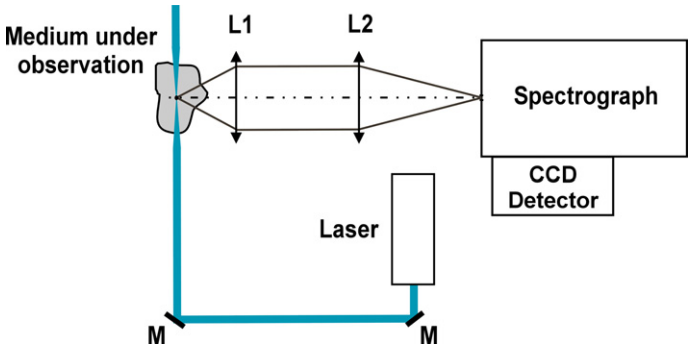


Fig. 5. Schematic diagram of the laser Thomson scattering apparatus.

532 nm and the scattering angle is 90°. Therefore, the experimental conditions of this study are well within the range of incoherent Thomson scattering. In that case, the Thomson scattered power per unit of frequency and within a solid angle $\Delta\Omega$ is expressed as

$$\frac{\mathrm{d}P_S}{\mathrm{d}\omega_S}\,\mathrm{d}\omega_S = P_i n_e L_{\mathrm{det}} \frac{\mathrm{d}\sigma_T}{\mathrm{d}\Omega}\Delta\Omega\, S_K(\Delta\omega)\,\mathrm{d}\omega_S \tag{2}$$

$S_k(\Delta\omega)\,\mathrm{d}\omega_s$ is the probability that the frequency shift of a scattered photon lies within a range $\mathrm{d}\omega_s$ around $\Delta\omega$. This equals the probability that the electron that scatters has a velocity component along $k$ within a range $\mathrm{d}v_k$ around the corresponding velocity $v_k = \Delta\omega/k$:

$$S_K(\Delta\omega)\,\mathrm{d}\omega_S = F_k(v_k)\,\mathrm{d}v_k \tag{3}$$

where $F(v_k)\,\mathrm{d}v_k$ is the one-dimensional electron velocity distribution along $k$. In terms of wavelengths rather than frequencies, this expression can be rearranged to

$$S_K(\Delta\lambda)\,\mathrm{d}\lambda_S = \frac{c}{2\lambda_i \sin(\theta/2)} F_k\left(\frac{c}{2\sin(\theta/2)}\frac{\Delta\lambda}{\lambda_i}\right)\mathrm{d}\lambda_s \tag{4}$$

In the case of a electron Maxwellian distribution, the incoherent Thomson scattering spectrum will be Gaussian in shape and therefore directly reflects the electron velocity distribution function in terms of per unit volume in velocity space, which is also Gaussian in form. $S_k(\Delta\lambda)$ will be then expressed as:

$$S_K(\Delta\lambda)\,\mathrm{d}\lambda_S = \left(\frac{m_e}{2\pi e T_e}\right)^{1/2}\left(\frac{c}{2\lambda_i \sin(\theta/2)}\right)\exp\left(\left(-\frac{m_e}{2eT_e}\right)\left(\frac{c\Delta\lambda}{2\lambda_i \sin(\theta/2)}\right)^2\right) \tag{5}$$

Electron temperature is related to the half width at half maximum according to:

$$\Delta\lambda_{T,1/2} = \frac{2\lambda_i \sin(\theta/2)}{c}\sqrt{\frac{2eT_e \ln 2}{m_e}}e \tag{6}$$

The electron density $n_e$ is obtained from Eq. (2) by calibrating the detection system in intensity. This absolute calibration is performed by using the Rayleigh or the Raman scattering measured on air at known thermodynamical conditions.

### *3.2. Electron number density and temperature measurements*

The Thomson scattering measurements are performed with the experimental setup composed of three components (Fig. 5). The first element consists of a frequency doubled Nd:YAG laser. The second component is the lens system focusing the laser beam inside the pulsed discharge. The third module concerns the detection system, which is based on the use of a triple grating spectrograph combined with an unintensified charge-coupled device (CCD), two lenses being also used to image the laser beam onto the slit of the spectrograph. A seeded frequency-doubled Nd:YAG laser (Quantel) is used as the light source. It delivers over 500 mJ of average power at 1064 nm and 200 mJ at 532 nm

with a pulse energy stability of 0.5% rms. This system operates at a pulse repetition rate of 10 Hz with a 13 ns pulse width and a spectral line width less than 0.003 $cm^{-1}$. The laser beam at 532 nm is focused within the pulsed discharge using a 500 mm focal length achromat. The Thomson scattering light is collected by an 80 mm focal length lens and imaged onto the spectrograph entrance slit by a 200 mm focal length lens. The probe volume is then assimilated to a parallelepiped volume whose dimensions result from the size of the entrance slit of the spectrograph, of the magnification of the collection optics and of the dimension of the focus spot of the green beam within the pulsed discharge. For the present experiment, the dimensions of the probe volume were equal to 1 mm long and 100 μm in diameter. The Raman spectrograph (Jobin–Yvon T 64000) has a 640 mm focal length and an f-number of 7.5. It is equipped with three 1800 grooves $mm^{-1}$ diffraction gratings allowing good rejection of the signals emitted at the excitation wavelength (Rayleigh scattering, Mie scattering and stray light). The Raman spectrum is detected by a back-thinned liquid nitrogen cooled CCD camera equipped with a 800 × 2000 chip (Jobin–Yvon Spectrograph). Its quantum efficiency reaches 85% at 500 nm. The dark current is lower than 3 $e^-$/pixel/hour and the readout noise is roughly 3–4 counts. The spectral resolution of the optical system is equal to the spectrograph resolution (∼0.003 nm/pixel). All the optical system is mounted on a high precision three-axis remotely-controlled traverse, allowing the displacement of the probe volume across the flow. The Thomson scattering setup is aligned by measuring the rotational Raman scattering spectrum in air. This spectrum is also used for the intensity calibration of the Thomson scattering measurements. By adjusting the positions of the different gratings and the widths of the slits located between the different gratings, the Thomson scattering spectrum is recorded on a spectral range of 200 $cm^{-1}$ located at less than 30 $cm^{-1}$ from the Rayleigh transition. No interference on the Thomson signal from the Rayleigh signal and the scattered laser light has been observed, demonstrating the excellent power rejection of light by this detection system.

Due to the weak Thomson scattering signals, data acquisition is performed by accumulating single-shot laser measurements triggered with any successive pulsed discharges. For the present experiment, the laser repetition rate used to record the Thomson scattering signals is fixed at 10 Hz and the laser energy is reduced to 10 mJ per pulse. Above this level of energy, interaction between the pulsed discharge with the laser beam is then observed with possible appearance of laser breakdown. The Thomson scattering spectrum is integrated over a period of 1 min in order to obtain a signal-to-noise ratio which allows the data reduction of the Thomson scattering signal. The peak intensity of the Thomson scattering signal is then typically equal to 500 photoelectrons. In order to suppress the light emission produced by the plasma and the stray light from the Thomson scattering signal, a specific experimental procedure was adopted. The experiment consists on recording first the plasma emission without any laser beam under the same experimental conditions in which Thomson scattering spectra are recorded. The Thomson scattered light added to the plasma emission is then recorded with the laser beam propagating within the plasma. The Thomson scattering spectrum is then obtained by subtracting the plasma emission and the stray light from the raw Thomson scattering signal. The absolute intensity of the Thomson signal is obtained using the rotational Raman scattering spectrum, which is recorded in air before each Thomson scattering measurement. The resulting Thomson scattering spectrum is then fitted using a least-squares method with theoretical predictions using a Gaussian profile for the electron velocity distribution function.

As an example of results, laser Thomson measurements were performed in air for several delays in the high-voltage pulse to assess to the temporal evolution of electron temperature and electron density during the current pulse. The results are displayed in Fig. 6. Measurements carried out at the current peak (i.e. $\Delta t = 20$ ns), yields to an electron temperature of about 2.6 eV and an electron density of $10^{15}$ $cm^{-3}$. These values, combined with room conditions of air where the plasma is produced ($P = 1$ bar and $T = 300$ K), allows to determine the four physical parameters required the description of the plasma. A Debye length of $3.7 \times 10^{-7}$ m, a mean gap between electron of $10^{-7}$ m, a Landau radius of $5.7 \times 10^{-10}$ m and an electron mean free path of $9.6 \times 10^{-4}$ m are then obtained. These values specify that this discharge can be classified into the "kinetic plasmas". Furthermore, the ionization factor, estimated to $4 \times 10^{-5}$ allows one to conclude that this plasma is weakly ionized. Complementary measurements performed at delays between 30 and 70 ns also show the fast decrease of electron temperature (from 2.6 to 1 eV) and the reduction of electron density by a factor of 10 (Fig. 7). This last data is in agreement with the reduction of electrical current by a factor of 8, demonstrating then the potential of LTS to measure the electron properties of these nanosecond pulsed discharges.

The agreement between the Thomson-scattering data and the corresponding fitted curves in Fig. 7 clearly suggests that free electrons in this discharge follow a Maxwellian velocity distribution under a broad set of sample conditions. In other words, the collisions between electrons are so frequent that fast heating of electrons in the pulsed discharge,

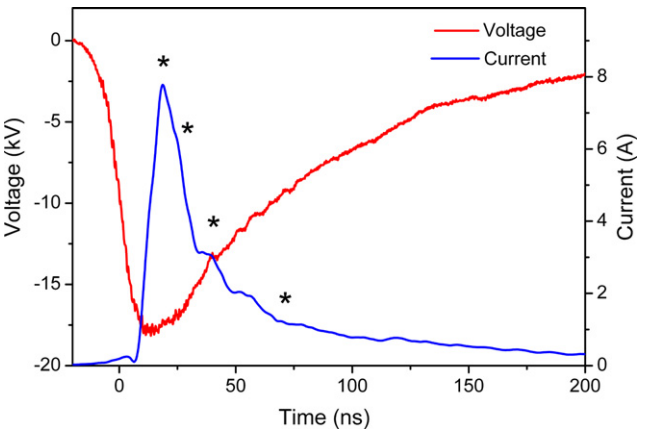


Fig. 6. Temporal locations of LTS measurements (*) in the current pulse.

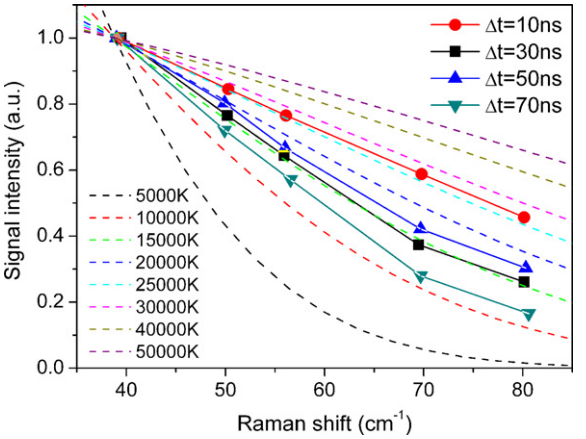


Fig. 7. Experimental-theory comparison of LTS signals versus the Raman shift from the laser wavelength.

collisions between electrons and heavy molecules and electron impact excitation process do not significantly affect the character of the electron energy distribution. Of course, is possible that the electron energy distribution might deviate slightly from a Maxwellian velocity distribution, but this small departure is within our current experimental error. Also, the fact that the discharge is weakly ionized and presents a small reduced electric field $(E/n)$ of 250 Td corroborate that the electrons, after creation, do not gain energy from the electric field but lose their energy in various collisions.

## 4. Thermal mechanisms

Coherent anti-Stokes Raman scattering (CARS) was used to measure the temporal evolution of the temperature of neutral molecules present in the discharge. In this study, nitrogen has been used as the probe molecule due to its abundance in the gas mixture.

### *4.1. CARS diagnostic*

The required hardware for CARS can be divided into three subsystems: the laser sources, handling optics and detection systems. The laser system is composed of two lasers which produce the pump and Stokes beams allowing $N_2$ thermometry. The frequency doubled output of a Nd:YAG laser composed of a single-mode Q-switched oscillator followed by an amplifier produces the pump beam. The laser delivers 200 mJ in 13 ns pulses with a repetition rate of 10 Hz, thus providing single-shot measurements that can be used to study the dependence/variability of a process. Half of the green energy is used to pump the Stokes dye laser which emits the broadband $\omega_S$ Stokes beam. Rhodamine 610 dye is diluted in ethanol to produce the Stokes beam centered at 607 nm with a 100 $cm^{-1}$ bandwidth (FWHM). At the output of the laser bench, the pump beam is split in two parallel beams and one of them is overlapped with the $\omega_S$ beam (planar BOXCARS geometry). The beam energy is 30 mJ/pulse for each of the pump beams and 4.5 mJ/pulse for the Stokes one. All the lasers are horizontally polarized. The laser beams are first focused in an atmospheric argon flow where a non-resonant CARS signal is created to monitor the shot-to-shot fluctuations of laser beam energy and the variations of the spectral shape of the Stokes laser. That reference signal is then split off and the laser beams are focused in the centre of the discharge by means of a 250 mm-focal-length achromatic lens. With a beam separation of 20 mm, the probe volume can be considered as a 0.8 mm-long and 40 μm diameter small cylinder. This probe volume is aligned along the longest dimension of the discharge in order to limit interference of the CARS signal induced by the discharge with $N_2$ CARS signal created in air surrounding the plasma (see Fig. 8). The focal beam is positioned axially and radially in the medium by moving the burner and the electrodes by means of translational stages. The resulting pump and Stokes beam energies are adapted for each measurement in order to prevent problems like laser-induced breakdown in the flowfield.

The $N_2$ CARS signal is sent to the detection system by means of mirrors. Reference and sample CARS spectra are dispersed using two separate spectrometers. The $N_2$ CARS spectrum and the broadband reference are formed in the

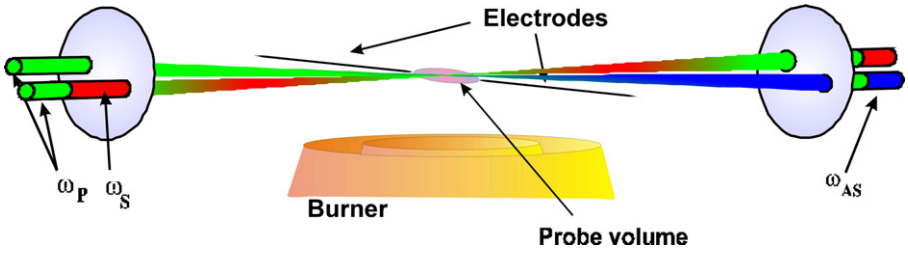


Fig. 8. Geometric arrangement of the CARS laser beams.

output plane of the spectrographs and detected by means of 512-photodiode arrays. The spectra are recorded in the spectral range 2330–2250 $cm^{-1}$ which allows the detection of the first three $N_2$ vibrational bands. Data acquisition are performed at a repetition rate of 10 Hz, and the laser beams are synchronized with the pulsed discharge using an external trigger delivered by the pulse/delay generator also used to trigger the pulsed discharge.

### *4.2. Results*

Investigation on the conversion of energy of the electrons on the different quantum states of nitrogen is performed in premixed $CH_4$/air mixtures. Characteristics of the discharge in terms of voltage and current pulses and repetitive rate remain unchanged. The equivalence ratio ($\Phi$) of the $CH_4$/air mixture was varied for surrounding the limits of ignition in order to separate the thermal processes produced by the discharge from those induced by combustion. The bulk flow velocity is fixed to 0.05 m/s. Typical results of rotational and vibrational temperature distributions as a function of time are displayed in Fig. 9.

In pure air, CARS measurements are only performed at $t \geqslant 40$ ns because of the strong production of electrons leading to randomly laser thresholds into the medium. A strong vibrational non-equilibrium is then observed with the presence of two vibrational temperature peaks. The first one is located within the discharge duration ($T_{vib} \geqslant 2200$ K) while the second one is measured at 20–30 μs ($T_{vib} = 1800$ K). The gas is heated up to 450–500 K except in the 5–200 μs period where a peak temperature of 900 K is measured. Complementary measurements at higher radial locations also reveal that the effect of the discharge on the gas flow disappears when the radial location exceeds 1 mm. A noticeable reduction of the vibrational non-equilibrium for short time delay (i.e. $t < 1$ μs) is first observed. Vibrational and rotational temperature peaks of respectively 800 K and 350 K at $r = 400$ μm decrease progressively to room temperature at $r = 800$ μm. For the 1–30 μs period, the increase of both temperatures subsists with an extent which depends on the radial location. We also note that the temperature peaks are moving up to longer time delays when increasing radial locations (typically 70 μs on a radial displacement of 800 μm). In the lean-regime condition (i.e., equivalence ratio ranging between 0 and 0.65), a considerable increase of both temperatures is then observed when adding $CH_4$ in the flowfield. We also observe a reduction of the extent of the vibrational non-equilibrium, which demonstrates the presence of a partial thermal equilibrium of the medium through the efficient energy transfer by collisions with $CH_4$ (or some of the decomposition products). The rotational and vibrational temperature distributions exhibit a quasi-flat profile over a period larger than 100 μs with a temperature peak of 2500 K for $\Phi = 0.65$, which allows the heating of the neutral molecules. Similar results are observed for rich $CH_4$–air mixtures. After a fast excitation of vibrational and rotational modes of $N_2$ leading to vibrational and rotational temperatures of respectively 3500 and 2750 K, relaxation of the populations of the excited vibrational and rotational states down to the ground state is observed at $t = 30$ μs. For $0.7 < \Phi < 1.3$, temperature up to 2400 K are measured which leads to the ignition of the $CH_4$/air mixture. While ignition seems to occur from the relatively fast increase of the rotational temperature after the high-voltage pulse, the rapid production of transient species with high concentration could also support this phenomenon. For that, the probe of OH and CH species in their ground state has been investigated within the discharge using PLIF technique.

## 5. Kinetic mechanisms

Another important property which can be considered is the propensity of the plasma to modify the chemical processes in the gas mixture. Unstable neutral particles such as radicals can be produced by the inelastic collisions

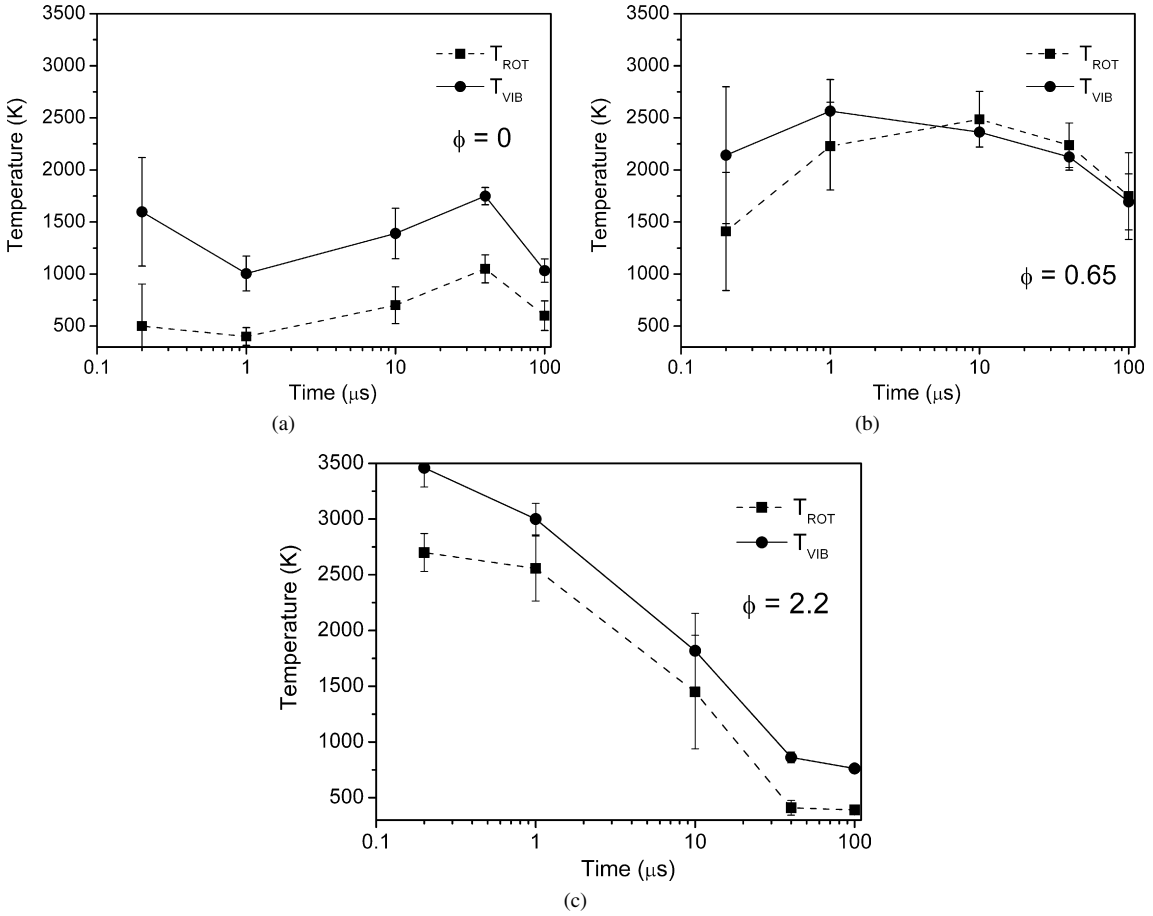


Fig. 9. Time evolution of (■) rotational temperature and (●) vibrational temperature for three equivalence ratio ($\Phi$).

between neutral molecules and electrons, and these species are extremely important in the improvement of combustion processes as previously observed. In order to evaluate these effects, the temporal distributions of OH and CH were measured by using Planar Laser-Induced Fluorescence (PLIF). Both molecules were selected in regard to their importance in combustion mechanisms. As for the CARS measurements, the measurements are performed for different equivalence ratios surrounding the limits of ignition in order to well isolate the chemical processes produced by the discharge from those induced by combustion.

### *5.1. PLIF apparatus for radical detection*

The laser system used for the PLIF measurements consists of a Nd:YAG laser (YG780, Quantel) combined with a dye laser (TDL 70, Quantel). For OH-PLIF measurements, the dye laser with Rhodamine 590 dye diluted in ethanol solvent is pumped by the Nd:YAG laser. The laser is tuned to the $Q_1(5)$ transition of the $(1,0)$ band of the $A^2\Pi^+$-$X^2\Sigma$ system of OH at 282.75 nm. Fluorescence from the $A$-$X(1,0)$ and $(0,0)$ bands is collected with an UV-Nikkor 105 mm/F4.5 lens and imaged onto an intensified CCD camera (PIMAX, 1024 × 1024 pixels). Dichroic and WG285 optical glass filters are used to detect fluorescence of OH radical in the 306–312 nm spectral range and to reject plasma emission and incident light. For CH-PLIF measurements, the $P_1(10)$ transition of the $C^2\Sigma^+$-$A^2\Pi(0,0)$ located at 317.30 nm is excited. This excitation wavelength is obtained using Rhodamine 610 diluted in ethanol solvent. Collection of fluorescence from the $C$-$X(0,0)$ band located between 313 and 318 nm is obtained by using a dichroic filter centred at 313 nm and presenting a HWHM of 5 nm. For both measurements, the laser beam is shaped into a 150 μm vertical sheet with 3 mm height, which corresponds to the distance between the two electrodes. Therefore, spatial resolution of PLIF is 20 μm × 20 μm × 150 μm. Optimization of the signal-to-noise ratio of the fluorescence signals

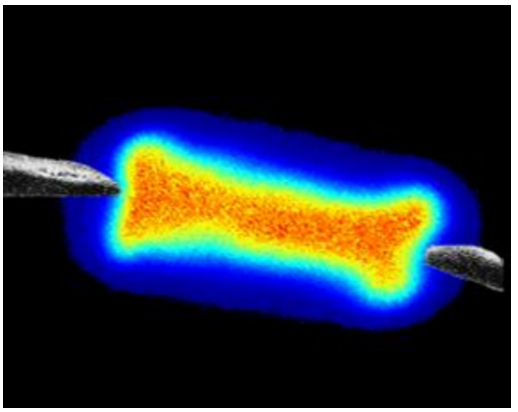

Fig. 10. Example of OH fluorescence distribution recorded between the electrodes at a delay of 20 µs.

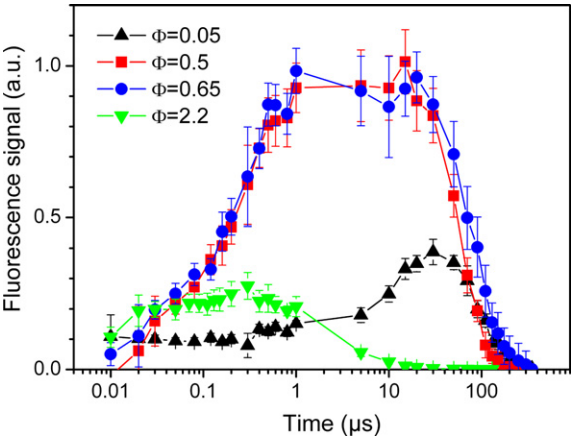


Fig. 11. Temporal evolution of OH fluorescence for various equivalence ratios.

is performed with an image intensifier gate of 20 ns. Energy in the laser sheet is fixed to 0.6 and 2 mJ for OH and CH experiments respectively.

### 5.2. *Radicals measurements*

Streamer-induced OH production was confirmed throughout the discharge volume located between the two electrodes. Fig. 10 shows a typical instantaneous OH distribution recorded over a cross section in the middle of the streamer at a delay of 20 µs after the high-voltage pulse. It is noted that OH production is quite homogeneous within the discharge. Observation of the OH spatial structures shows disturbances close to the electrodes which probably arise from additional electrically-enhanced surface catalytic reaction and/or local joule heating of the electrode enhancing the heat release.

From the fluorescence images recorded at various delays, the temporal evolution of OH fluorescence has been deduced for four equivalence ratio and the results are presented in Fig. 11. First of all, OH production is observable at a time less than 10 ns for very fuel lean regimes ($\Phi = 0.05$). This species subsists at similar concentration until $\Delta t = 1$ µs. After this period, a significant increase of OH is observed with a peak at 20–30 µs. Then, the OH fluorescence decreases and totally disappears after $\sim$200–300 µs. In the lean-regime condition (i.e., equivalence ratio ranging between 0.5 and 0.65), a considerable increase of OH fluorescence is also observed when adding $CH_4$. The OH fluorescence increases continuously to a delay ranging between 500 ns and 1 µs, then OH distributions exhibit a flat profile over a period larger than 30 µs. This delay, characteristic of the presence of peaks of OH and temperature, represents favorable conditions of the ignition of the fresh gases when increasing the equivalence ratio to 0.7. Finally, relaxation of OH population to the ground state is finally noted. Compared to the $\Phi = 0.05$ case, the maximum amount of OH is multiply by a factor of 10–12 demonstrating then the high reactivity of the plasma to produce a large amount of OH radicals. In the rich $CH_4$–air mixture, a fast production of OH is still observed until $\Delta t = 20$ ns. Then OH fluorescence exhibits a flat profile over a period of 800 ns and finally decreases continuously until $\sim$20–30 µs. Comparison of these OH temporal distributions with temperature measurements performed in similar conditions shows a strong correlation. In the very lean regime, a common increase of the OH production and rotational temperature which could arise from exothermic recombination reactions with transient species like O or H atoms is noted. In a lean regime ($0.5 < \Phi < 0.65$), similar correlations between temperature and OH production are also observed. The simultaneous increase of the peaks of OH and temperature indicates exothermic plasma chemical fuel oxidation triggered by radicals produced within the discharge which results in flow heating up to 2500 K. Finally, the fast decrease of OH in the rich $CH_4$–air regime is piloted by the large relaxation of energy into the plasma.

A preliminary experiment of CH detection using PLIF was also performed in the same conditions than for OH experiment. CH production is also observed within this plasma, indicating efficient decomposition of fuel by the plasma. For instance, Fig. 12 shows a typical instantaneous CH distribution recorded on a cross section in the middle of the discharge. This measurement was recorded at a delay of 500 ns after the high-voltage pulse. Contrary to the

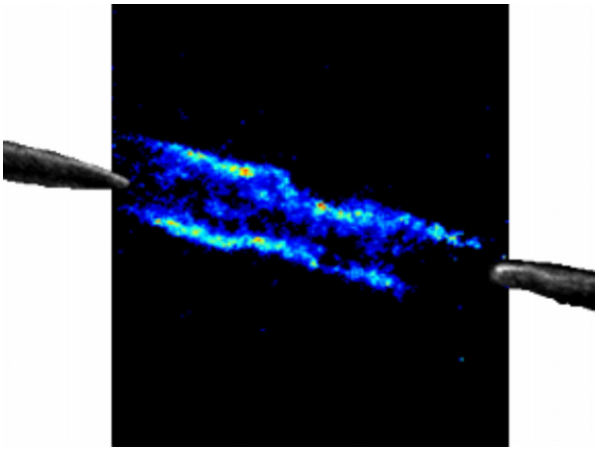

Fig. 12. Example of CH fluorescence distribution recorded between the electrodes at a delay of 500 ns.

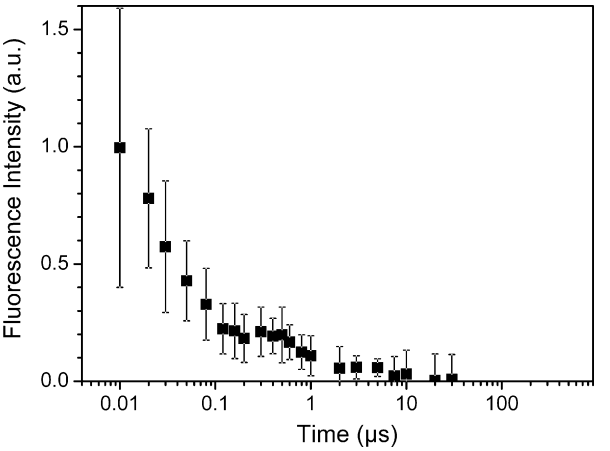


Fig. 13. Temporal evolution of CH fluorescence for an equivalence ratio of 2.2.

OH case, the distribution of CH fluorescence is not uniform in volume between the electrodes. The presence of CH is observed in two very thin zones located at the periphery of the plasma sheath. Analyzing the CH fluorescence images with the same method as for OH allows the measurement of the temporal behavior of CH fluorescence. Fig. 13 shows, for instance, the temporal evolution for the rich $CH_4$–air mixture case. After a strong production of CH at a delay less than 10 ns, the CH fluorescence signal decreases progressively until $\Delta t = 100$ ns. A flat profile with a small rising of CH at $\sim$500–600 ns is then observed. After this delay, CH continues to decrease and totally disappears after $\sim$10–20 μs due to its strong quenching with temperature. The temporal behavior of CH production, with however a reduction of the total CH intensity, remains similar when approaching the equivalence ratio relating to the upper limit of ignition (i.e. $\Phi = 1.3$). The small peak of CH observed at $\sim$500–600 ns is then, as for the OH radicals, a good indicator of the presence of a strong reactivity of the mixture which expresses the opportunity to ignite the gas mixture.

## 6. Conclusion

Detailed experimental investigation of a non-equilibrium nanosecond pulsed discharge in premixed $CH_4$/air mixtures at atmospheric pressure has been carried out. A needle-to-needle geometry with a gap of 3 mm has been used with the following high-voltage pulse parameters: the pulse amplitude is 20 kV, the FWHM duration is 70 ns, the rise time is 20 ns and the repetition rate is 100 Hz. The experiments demonstrated the possibility to improve the combustion properties of a premixed $CH_4$/air flame. The transient plasma has consistently shown significant reductions in ignition delay and increased lean burn capability relative to conventional spark ignition. Through advanced laser diagnostics measurements, we have identify the physical processes which lead to these improvements. In a first step, the characterization of the electric properties of the plasma, i.e. electron temperature and electron density which are known as the key parameters for a reliable classification of this kind of plasma was performed. This work has been successfully performed by using laser Thomson scattering (LTS). Then, temperature measurements were performed using nitrogen CARS thermometry. These measurements intended to quantify the energy transfer in the gas mixture. Spatial and temporal evolution of temperature distributions was recorded by delaying the probe lasers relative to the discharge pulse in the range 10 ns–1 ms. It was demonstrated that energy transfer induced by collisions of $N_2$ with $CH_4$ considerably increases the thermal heating of neutral molecules at temperatures up to 2500 K. Effect of the discharge on the local temperature allows to ignite the $CH_4$/air mixture for equivalence ratio between 0.7 and 1.3. Fast development of a flame kernel is then observed. The experiment also shows that the flame can be sustained above the discharge due the repetitive ignition of the flame at the plasma repetition rate. Finally, OH and CH PLIF experiments were performed and intense OH and CH streamer-induced production was confirmed over the streamer volume. Additionally, it was demonstrated that OH produced by the nanosecond pulsed discharge decays to negligible values at a delay longer than 200 μs from the high-voltage pulse while CH is only produced on a time domain of 20–30 μs after the discharge. Future work will be devoted to quantify these radical productions in order to elaborate kinetic mechanism modeling. This work will be completed by probing O and H atoms which also plays a key role in the

mechanism of plasma assisted oxidation and ignition of $CH_4$/air flows. Furthermore, nanosecond pulse discharge will be implemented on an aircraft injection system in order to quantify the influence of the plasma on spray properties and combustion efficiency.

## Acknowledgements

This work was supported by Direction générale de l'armement which is gratefully acknowledged.

## References

[1] A. Bogaerts, E. Neyts, R. Gijbels, J. Van der Meulen, Gas discharge plasmas and their applications, Spectrochim. Acta Part B 57 (2002) 609–658.
[2] C.H. Kruger, C. Laux, L. Yu, D. Packan, L. Pierrot, Nonequilibrium discharges in air and nitrogen plasmas at atmospheric pressure, Pure Appl. Chem. 74 (2002) 337–347.
[3] S.M. Stariskovskaia, A.Yu. Stariskovskii, D.V. Zapsepin, Hydrogen oxidation in a stochiometric hydrogen–air mixtures in the fast ionization wave, Combust. Theory Modelling 5 (2001) 97–129.
[4] A.Yu. Starikovskii, Plasma supported combustion, Proc. Combust. Inst. 30 (2005) 2405–2417.
[5] S.M. Starikovskaya, Plasma assisted ignition and combustion, J. Phys. D: Appl. Phys. 39 (2006) R265–R299.
[6] S.A. Bozhenkov, S.M. Starikovskaya, A.Yu. Starikovskii, Nanosecond gas discharge ignition of $H_2$ and $CH_4$ containing mixtures, Combust. Flame 133 (2003) 133–146.
[7] E.I. Mintoussov, S.V. Pancheshnyi, A.Yu. Starikovskii, Propane–air flame control by non-equilibrium low-temperature pulsed nanosecond barrier discharge, AIAA Paper 2004-1013, 42nd AIAA Aerospace Sciences Meeting and Exhibit, Reno, NV, 2004.
[8] W. Kim, H. Do, M.G. Mungal, M.A. Cappelli, Optimal discharge placement in plasma-assisted combustion of a methane jet in cross flow, Proc. Combust. Inst. 31 (2007) 3319–3326.
[9] D. Galley, G. Pilla, D. Lacoste, S. Ducruix, C. Laux, Plasma-enhanced combustion of a lean premixed air–propane turbulent flame using a nanosecond repetitively pulsed plasma, AIAA Paper 2005-1193, 43rd AIAA Aerospace Sciences Meeting and Exhibit, Reno, NV, 2005.
[10] S. Pancheshnyi, D.A. Lacoste, A. Bourdon, C. Laux, Ignition of propane–air mixtures by a sequence of nanosecond pulses, AIAA Paper 2006-3769, 37th AIAA Plasmadynamics and Lasers Conference, San Francisco, CA, 2006.
[11] G. Lou, A. Bao, M. Nishihara, Ignition of premixed hydrocarbon–air flows by repetitively pulsed nanosecond pulse duration plasma, Proc. Combust. Inst. 31 (2007) 3327–3334.
[12] A. Bao, Yu.G. Utkin, S. Keshav, G. Lou, I.V. Adamovich, Ignition of ethylene–air and methane–air flows by low-temperature repetitively pulsed nanosecond discharge plasma, IEEE Trans. Plasma Sci. 35 (2007) 1628–1638.
[13] D. Messina, B. Attal-Trétout, F. Grisch, Analysis of a non-equilibrium pulsed nanosecond discharge at atmospheric pressure using coherent anti-Stokes Raman scattering, Proc. Combust. Inst. 31 (2007) 825–832.
[14] M.D. Bowden, Y. Goto, H. Yanaga, P.J.A. Howarth, K. Uchino, K. Muraoka, Plasma Sources Sci. Technol. 8 (1999) 203–209.
[15] J. Sheffield, Plasma Scattering of Electromagnetic Radiation, Academic Press, New York, 1975.
[16] K. Muraoka, K. Uchino, M.D. Bowden, Diagnostics of low-density glow discharge plasmas using Thomson scattering, Plasma Phys. Control. Fusion 40 (1998) 1221–1239.
[17] H. Kempkens, J. Uhlenbusch, Scattering diagnostics of low-temperature plasmas (Rayleigh scattering, Thomson scattering, CARS), Plasma Sources Sci. Technol. 9 (2000) 492–506.